Learning In-Hand Translation Using Tactile Skin With Shear and Normal Force Sensing

Jessica Yin[1,2] **Haozhi Qi**[1,3] **Jitendra Malik**[1,3] **James Pikul**[4] **Mark Yim**[2] **Tess Hellebrekers**[1]

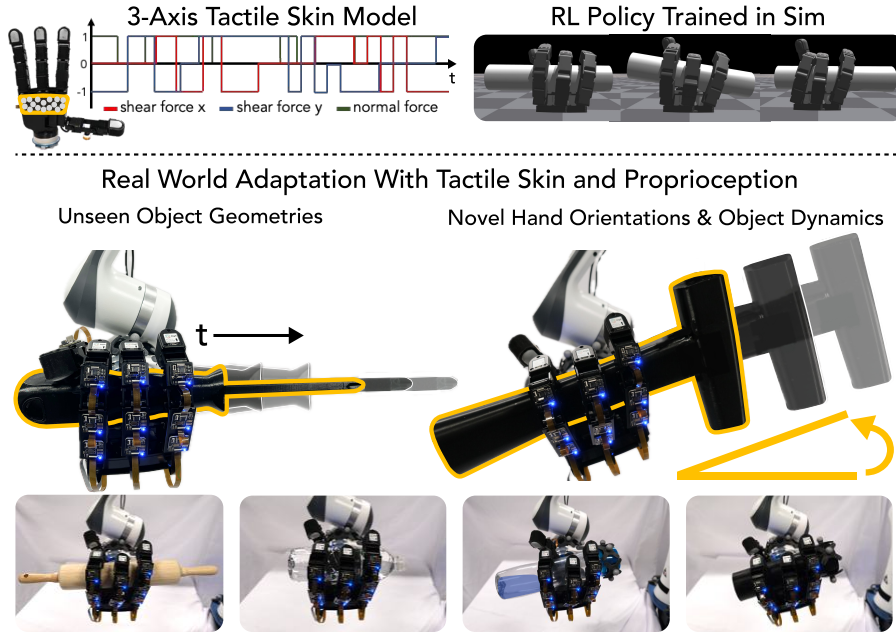[1]Meta FAIR   [2]University of Pennsylvania GRASP Lab   [3]UC Berkeley   [4]UW-Madison

Figure 1: We present a tactile skin model that enables *zero-shot* sim-to-real transfer of ternary shear and binary normal forces. We use it to learn an RL policy for dexterous in-hand translation that uses tactile and proprioceptive feedback to adapt to unseen object geometries, novel hand orientations, and new object dynamics. We evaluate our policies with over 190 real-world rollouts. More videos are at our project website.

Abstract: Recent progress in reinforcement learning (RL) and tactile sensing has significantly advanced dexterous manipulation. However, these methods often utilize simplified tactile signals due to the gap between tactile simulation and the real world. We introduce a sensor model for tactile skin that enables *zero-shot* sim-to-real transfer of ternary *shear* and binary *normal forces*. Using this model, we develop an RL policy that leverages sliding contact for dexterous in-hand translation. We conduct extensive real-world experiments to assess how tactile sensing facilitates policy adaptation to various unseen object properties and robot hand orientations. We demonstrate that our 3-axis tactile policies consistently outperform baselines that use only shear forces, only normal forces, or only proprioception.

Keywords: Tactile Sensing, Sim-to-Real, Dexterous Manipulation

1   Introduction

Humans rely on their sense of touch to manipulate objects throughout their daily lives [1]. Inspired by this, a prominent area of manipulation research focuses on equipping robots with tactile sensors [2, 3]. However, despite the development of capable tactile sensors [4, 5, 6], there remains a significant gap between the breadth of information they can capture and what state-of-the-art robot controllers can utilize for feedback. Recently, reinforcement learning (RL) and sim-to-real

techniques have enabled breakthroughs in integrating tactile feedback into low-level controllers for dexterous manipulation [7, 8, 9]. However, these are constrained by the speed and accuracy of tactile simulation techniques and often rely on simplified tactile signals. Although tactile simulation has been actively pursued recently [10, 11, 12], simulating rich, large-area, and high-fidelity tactile sensing with high throughput remains a challenge.

Tactile sensors approximate contact through soft body deformation, which is traditionally modeled using slow and high-fidelity techniques like FEM [13, 14, 15]. At the other extreme, most simulators fast enough to train RL controllers use overly simplified contact models for numerical stability, which struggle to bridge the sim-to-real gap. Robotic dexterity requires a balance between simulation speed and fidelity to fully leverage the progress in both tactile sensing and RL techniques. To that end, we introduce a tractable tactile skin model that outputs binary normal and shear forces at 5000 FPS on two GPUs, achieving 70% of the speed of training a proprioception-only policy. We demonstrate the fidelity of the proposed tactile sensor model through zero-shot sim-to-real transfer of policies trained entirely in simulation.

We focus on in-hand translation of objects across the palm. In-hand translation is useful for practical applications such as repositioning tools to a specific grasp, and is also challenging because it requires controlled sliding of the objects [16, 17, 18]. We choose this task specifically to better investigate the utility of our ternary shear outputs in improving policy performance. With current limitations in simulating contact dynamics and tactile skin, we have yet to see examples of this dexterous skill with tactile feedback including shear forces.

In summary, we introduce our sim-to-real approach for in-hand object translation using tactile sensing. We make three key contributions:

- To the best of our knowledge, we contribute the first RL-tractable sensor model for compliant tactile skin that enables *zero-shot* sim-to-real transfer of binary normal *and shear* signals.
- We use our three-axis sensor model to learn RL control policies for in-hand translation, a dexterous, contact-rich task that requires controlled sliding contact.
- We evaluate our control policies with 190 *real-world* rollouts and show that policies with three-axis tactile sensing achieve superior in-domain task performance and adaptation to unseen objects and hand orientations.

2 Related Work

Tactile Sensor Simulation. The crux of tactile sensor simulation is efficiently and sufficiently modeling the deformations and forces at the soft contact interface. Most works focus on simulating fingertip visuo-tactile sensors, which use cameras to observe soft material deformations upon contact [10, 19, 20]. Finite Element Method (FEM)-based approaches are high fidelity [21, 22, 23], but their computational cost prevents their use in RL policy learning. Si et al. [12] uses FEM to demonstrate a sim-to-real RL policy for two-fingered grasping, but the tractability may not extend beyond this small action space. Tacto [11], Mujoco [24], and IsaacGym [25] use collision geometry penetration to efficiently estimate forces. While this can be sufficiently accurate for normal forces, it produces sparse signals for shear. Xu et al. [10] leverages rigid-body assumptions in tactile modeling for sim-to-real, but assumes constant and sticking contact, and other contact modes are not demonstrated.

Far fewer recent works explore non-camera based tactile skin simulation [26, 27]. These approaches decouple deformation modeling and sensor response to account for cross-talk and noise, producing realistic data but suffering from intractability for RL policy training. Yin et al. [8] simulates force-sensitive resistors as binary tactile sensors using the default IsaacGym tactile sensor model. In contrast, our work introduces a simulation model for both normal and shear forces for a magnetic tactile skin [6, 28].

In-Hand Manipulation. In-hand manipulation has been studied for decades using either classical control [18, 29, 30, 31, 32, 33, 34, 35] approaches or learning-based methods. Learning-based methods can be categorized to real-world imitation learning [36, 37, 38, 39, 40] and sim-to-real with reinforcement learning [41, 42, 43, 44, 45]. Our method falls into the latter category and
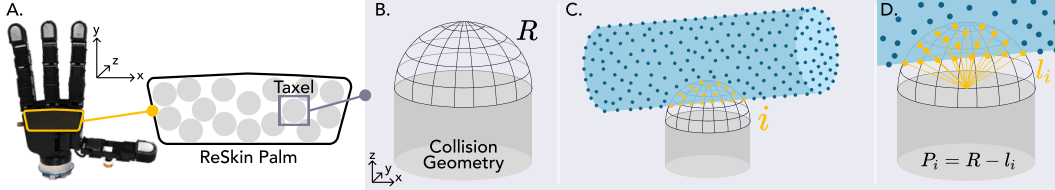
Figure 2: **Our modeling approach for sim-to-real transfer of tactile skin.** A) We model the palm as a continuous surface with 16 discrete taxels, each corresponding to an underlying magnetometer. B) We use a cylinder for each taxel and extend the sensing range (R) beyond its collision geometry. C) We sample points on the object and represent the collision surface as a point cloud. Points within sensing range are denoted as i. D) We sum the penetration distances $P_i = R - l_i$, where l_i is the distance from point i to the sensor's origin. We calculate the sensor signals for shear and normal force using $\sum_{i=1}^{n} P_i$, object velocity, and object point density.

differs from existing work from two perspectives. First, the majority of existing methods focus on in-hand object reorientation [7, 8, 46, 47] while our work focuses on in-hand object translation. This task is a complementary skill with in-hand rotation, and a critical step towards general in-hand manipulation. Second, most existing learning-based in-hand manipulation systems use vision [44] and proprioception [46], or simplified touch sensing limited to normal forces [7, 8]. In contrast, our touch sensing pipeline provides both shear and normal forces for controller feedback.

3 Tactile Skin Model

Our sensor model focuses on ReSkin [6], a magnetic elastomer tactile skin, which we adhere to the palm of the robot hand (Figure 2A). As the skin deforms and the positions of the embedded magnetic particles change, underlying magnetometers measure the magnetic flux as a proxy for 3-axis force. To minimize the effects of hysteresis and cross-talk, we binarize the sensor outputs in both simulation and reality. We implement our tactile sensor model and train our RL policy in IsaacGym [25], and it achieves around 70% of training speed compared to training without any tactile sensors. For context, with 2 NVIDIA RTX-4090 GPUs, we get 5000 FPS training with tactile sensors and approximately 7000 FPS without tactile sensors.

Our approach contrasts with the default tactile sensor models offered in simulators such as Mujoco and IsaacGym, which report normal and shear signals calculated primarily from collision geometry penetration (Figure 3). Although this approach offers numerical stability in simulation by neglecting rapid changes in frictional forces, it produces sparse and unrealistic signals for shear forces in tactile sensor models. Our sensor model outputs sufficiently accurate shear and normal forces for sim-to-real transfer, while still leveraging the speed and stability of the simulator by using collision geometry penetration to calculate dynamics and contact interactions.

3.1 Discretization

The ReSkin palm is modeled in two parts. First, we model the ReSkin palm pad as a rigid volume with the same physical dimensions as the real sensing skin. The simulated ReSkin palm pad acts as a continuous collision surface for more accurate dynamics during the task. Second, although ReSkin is continuous, we discretize the sensing skin to 16 discrete taxels, each corresponding to the location of an underlying magnetometer (Figure 2A). We model each ReSkin taxel as a cylinder collision geometry ($r = 1.5$ cm), placed coincidentally on the surface of the ReSkin palm.

3.2 Compliance

We use two techniques to model the compliance of ReSkin: 1) extending each sensor's range beyond its collision geometry, and 2) representing the manipulated object as a point cloud, with each point contributing to the tactile sensor signal. Extending the sensing range beyond its geometry allows for sensor activation by object "contact" without collision (Figure 2B). This mimics an interaction with a compliant volume by not exerting a large reaction force on the object. For the object point cloud, we uniformly sample only from the object surface to represent the contact geometry. For object points within the sensing range, the penetration distances directly scale the sensor signal (Figure
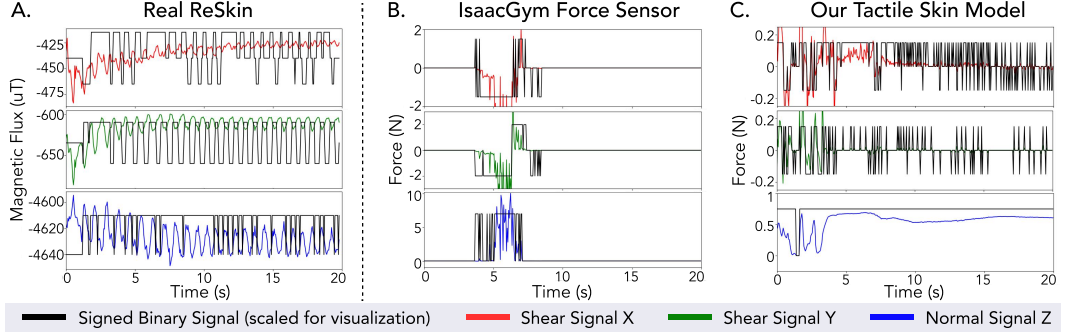
3

Figure 3: **Tactile signal comparisons during an entire episode of in-hand translation.** A) A representative example of **real-world** ReSkin palm taxel output. The signals are periodic because the finger gait is periodic. B) The force sensor output of a **simulated** palm taxel, using the default IsaacGym force sensor model similar to [8, 47]. The signals are sparse because the model relies on collision geometry penetration. C) The taxel outputs from our **simulated** S3-Axis tactile skin model, for the *same taxel* and the *same rollout* as B.

2C-D). This technique allows us to calculate tactile signals that correspond with intersecting contact *volumes*, in contrast to using the typical single *point* per two body collision approximation.

3.3 Shear and Normal Sensor Signals

To calculate shear signals, we draw inspiration from Coulomb models of sliding and rolling contact [48] that scale tangential forces with normal force and object velocity. We use: $S_{x,t} = \frac{\sum_{i=1}^{n} P_i}{D}(v_{x,t} + \omega_{x,t})$ and $S_{y,t} = \frac{\sum_{i=1}^{n} P_i}{D}(v_{y,t} + \omega_{y,t})$ where x and y correspond to global coordinate axes and are tangential to the sensor surface, $S_{x,t}$ and $S_{y,t}$ are the shear signals produced by each taxel, $v_{x,t}$ and $v_{y,t}$ are the linear velocities of the object, $\omega_{x,t}$ and $\omega_{y,t}$ are the angular velocities of the object, $\sum_{i=1}^{n} P_i$ is the summation of object point penetration distances within the sensing range, and D is the object point density (total number of object points divided by object volume). The point penetration distance is the L_2 norm of sensor range and the 3D object point coordinates. For the normal force signal, we use $S_{z,t} = \frac{\sum_{i=1}^{n} P_i}{D}$. We calculate the normal force with the summation of object point penetration distances, divided by object point density. The object point penetration distances are a proxy for normal force. Dividing by object point density accounts for different scales of the object.

To bridge the reality gap, we train the control policy with thresholded sensor signals from our tactile skin model: $S_{x,t} \in \{-1, 0, 1\}, S_{y,t} \in \{-1, 0, 1\}$, and $S_{z,t} \in \{0, 1\}$. For the signed 3-axis policy variant (*S3-Axis*), we retain positive and negative signs of shear signals, which give direction along each axis. For the unsigned 3-axis policy variant (*U3-Axis*), we take the absolute value of the shear signal. Additionally, $S_{x,t}, S_{y,t} = 0$ if $v_{x,t}, v_{y,t}, \omega_{x,t}, \omega_{y,t} = 0$. Although this neglects potentially nonzero friction forces while velocities are 0, it reflects how real ReSkin signals are binarized.

3.4 Real-World Binary Tactile Processing

Raw signals from ReSkin have significant hysteresis, such that simple thresholding is not sufficient for binarization. Instead, we use a threshold on the *time derivative* of the signal. We use two buffers: one for signal history and one for the current signal. If the difference between the signal history and current signal buffers exceeds the threshold, then a 1 or -1 is returned (else 0). We tune buffer sizes and thresholds per x, y, z axis. There is a slight delay in binary sensor outputs due to the dependence on signal history, but because ReSkin outputs data four times faster (78 Hz) than the policy sampling rate (20 Hz), we find this delay to be negligible. Additionally, using the time derivative means that if there is no signal change, the binarization algorithm will eventually output 0. We make this trade-off in our binarization algorithm to cope with hysteresis; however, in practice, this scenario is rare because the object is typically in motion and causes frequent signal changes.
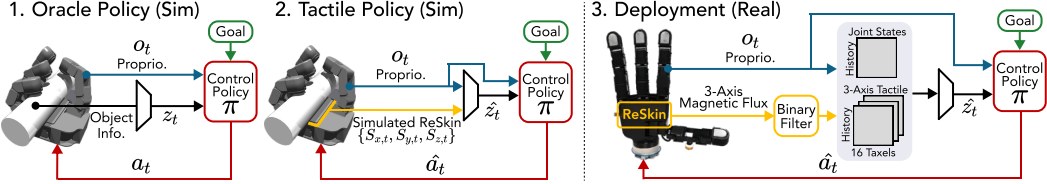
4

Figure 4: **Overview of our training and deployment pipeline.** We train the policy in two stages, entirely in simulation. We use our tactile skin model in the second stage. The policy is directly deployed in the real world.

4 Learning In-Hand Translation with Tactile Skin

To demonstrate the effectiveness of our simulated tactile skin model, we perform sim-to-real experiments on the in-hand translation task. This task requires rich, controlled sliding contact on the palm, so we hypothesize that palm tactile feedback can be particularly useful.

Oracle Policy Learning. We adopt a two-stage method for policy learning from [46, 7]. First, we train an oracle policy π with privileged information openly available from the simulator. Second, we train the tactile policy with an observation encoder using our simulated sensor model and freeze the control policy π. During deployment, we directly deploy the control policy and observation encoder in the real world. An overview is shown in Figure 4.

The privileged information includes object state and physical properties sampled from the simulator. This information includes object position, velocity, size, mass, center of mass, and coefficient of friction. It is then encoded in an 8-dimensional vector, z_t, representing information that the policy finds useful and relevant for the task. The inputs to the oracle policy, π, are finger joint positions from proprioception and the encoded privileged information, z_t. The policy outputs the 16 joint position targets of the PD controller, $a_t \in \mathbb{R}^{16}$. The observation o_t contains a temporal window of joint positions and actions, $o_t = [q_t, a_t] \in \mathbb{R}^{96}$. This gives us $a_t = \pi(o_t, z_t)$.

The task requires the control policy to translate objects in one direction across the palm. Our reward function uses penalties on object state to specify the in-hand translation task and penalties on robot behavior to produce finger gaiting. The reward contains three main terms: task rewards ($r_{\mathrm{iht}}, r_{\mathrm{goal}}$) to define the task, motion penalties ($r_{\mathrm{rotp}}, r_{\mathrm{pose}}$), and energy penalties ($r_{\mathrm{work}}, r_{\mathrm{torque}}, r_{\mathrm{force}}$). Please see the Appendix for the detailed reward formulation. We use PPO [49] to optimize the oracle policy and share weights between the policy and the critic network. An extra linear projection layer estimates the value function. During training, a cylinder with randomized physical properties is initialized in a stable grasp for each environment and we assign a random goal position to the environment.

Tactile Policy Learning. The key difference between the oracle policy and the tactile policy is the observation encoder. We concatenate simulated sensor data from proprioception (q_t) and our tactile skin model ($[S_{x,t}, S_{y,t}, S_{z,t}]$) as inputs to the observation encoder. The observation encoder is a transformer trained to minimize the L_2 norm between: 1) z_t and $\hat{z}_t$, aiming to replicate the privileged representation from simulated sensor data, and 2) a_t and $\hat{a}_t$, aiming to replicate the same actions as the oracle control policy.

5 Experiment Setup

Hardware Setup. We use an Allegro Hand [50] for our experiments. It has four fingers, each with four degrees of freedom (DoF). The 16 joints receives target joint position from neural network controller at 20 Hz, and the commands will be converted to torque using a PD controller at 300 Hz. ReSkin, measuring approximately 37 mm x 96 mm, is adhered to the palm of the Allegro Hand and outputs tactile data in $\mathbb{R}^{16 \times 3}$ at 78 Hz. Since there is high friction between the objects and ReSkin, the ReSkin palm is covered with a 0.25 mm sheet of PET-like plastic to reduce the required torque from the robot fingers for the task, thus avoiding overheating.

Simulation Setup. We use the IsaacGym [25] simulator to train our policy. Each environment contains a robot hand and randomly scaled cylinder (Figure 5). We use our model from Section 3 to

5

simulate tactile data. The simulation frequency is $200\,\mathrm{Hz}$, and the control frequency is $10\,\mathrm{Hz}$. Each episode lasts 400 time steps ($20\,\mathrm{s}$) and resets when the object falls.

Ablations. We ablate tactile modalities to compare our methods, *Signed 3-Axis (S3-Axis)* and *Unsigned 3-Axis (U3-Axis)*. All policies are trained with the same oracle policy, and all tactile policies use proprioception and 16 palm taxels.

Figure 5: **Train and test sets.** We train with cylinders and no hand tilt in simulation. We test on real objects with varying COM, geometries, and hand angles. Motion capture markers on the objects are only for measuring task metrics.

1. *Signed Shear Only.* The tactile sensors only output ternary values for shear forces: $S_{x,t}, S_{y,t} \in \{-1, 0, 1\}$ and $S_{z,t} \in 0$.
2. *Normal Only.* The tactile sensors only output binary values for normal forces: $S_{x,t}, S_{y,t} \in \{0\}$ and $S_{z,t} \in \{0, 1\}$. This baseline is similar to [8].
3. *Proprioception Only.* The policy is trained without tactile sensors.

Metrics. We use the following metrics to measure policy performance. We use Optitrack motion capture to track object pose at $240\,\mathrm{Hz}$ to calculate these metrics. For all metrics, higher is better.

1. *Success Rate.* Success is defined as the policy achieving an object translation distance greater than 0 mm within 120 s. We set the threshold to be 0 mm because some policies completely fail to move the object or drop it, especially when the hand is tilted.
2. *Average Object Distance.* The average maximum distance (cm) an object moves along the desired translation axis, calculated from successful rollouts.
3. *Average Object Velocity.* The average object velocity (cm/s) along the desired translation axis, calculated from successful rollouts.

Object Dataset. We evaluate policies with the following in-domain (ID) and out-of-domain (OOD) objects. Our test set consists of real objects only: cylinder (ID), hammer (OOD, skewed COM), screwdriver (OOD, challenging geometry), and water bottle (OOD, variable COM) (Figure 5). More object details are in the Appendix.

6 Results and Analysis

An overview of our deployment pipeline is shown in Figure 4, and notably, *all evaluations are conducted in the real world*.

We first test in-domain policy performance on the canonical cylinder object, to compare Proprio-Only and a 3-axis tactile policy. Then, with the same cylinder, we test policy adaptation to OOD hand tilt angles *against* gravity. These tilt angles passively bias object motion opposing the desired translation direction, thus requiring more force from fingers and gait adaptation to complete the task. This experiment isolates the effect of tilting the hand. Finally, we test policy adaptation to OOD objects *and* hand tilt angles. We are interested in the limits of policy adaptation, so experiments focus on the maximum angles at which policies are still capable of completing the task.

6.1 Tactile Sensing Boosts In-Domain Task Performance and Adaptation to OOD Hand Tilt

First, we evaluate the performance of S3-Axis and Proprio-Only policies with the same setting as in training: translate a cylinder with no hand tilt (Figure 6A). We deploy 5 real-world rollouts for each policy. The S3-Axis policy achieves an increase of 38% translation distance (+2 cm) and 94% greater object velocity (+0.16 cm/s) compared to the Proprio-Only policy. Additionally, the S3-Axis policy performs more consistently, with lower standard deviations for both task metrics.

Next, we test the effect of hand tilt, an OOD condition that increases the object's tangential force opposing the desired direction of translation. We test hand tilts from 0-15 degrees in increments of 5 degrees. As shown in Figure 6A, the translation distance and object velocity generally decrease as the tilt angle increases. This indicates that task difficulty increases with hand tilt. The finger gait adaptations are less effective and the policy is slower to find effective adaptations to OOD physics. However, S3-Axis still outperforms Proprio-Only in both task metrics, across all tilt angles.
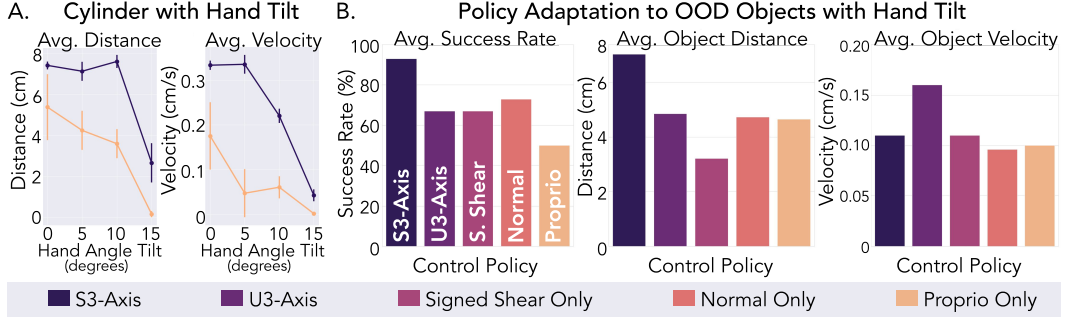
Figure 6: **A. Real-world cylinder rollouts with S3-Axis and Proprio-Only**. This shows superior S3-Axis policy performance compared to Proprio-Only for both ID and OOD conditions. Error bars indicate standard deviation. **B. Three-axis tactile sensing policies demonstrate the best adaptation to OOD objects and unseen hand orientations.** S3-axis enables **93% average success rate** and **+51% increase** in distance over Proprio-Only. U3-axis enables **+60% increase** in velocity over Proprio-Only. These metrics are averaged over all real-world OOD experiments (30 rollouts/policy).

6.2 Three-Axis Tactile Sensing Enables Superior Out-of-Domain Adaptation

In this section, we simultaneously test policy adaptation to two classes of perturbations: hand angle tilt *and* OOD objects. The three-axis tactile sensing policies achieve the best policy adaptation. We benchmark our results against Signed Shear Only, Normal Only, and Proprio-Only. In the remaining section and Figure 6B, we show that across all OOD experiments, S3-Axis and U3-Axis policies achieve, on average, superior performance compared to the other baselines. In Figure 7A, we highlight interesting cases. Full experimental results are in the Appendix.

Screwdriver - Challenging Geometry - No Hand Tilt. We evaluate our policy on the challenging screwdriver object. The screwdriver is highly nonuniform, featuring distinctly discontinuous surfaces that create multiple points of contact with the palm. This leads to very different tactile signatures compared to the training distribution. All policies are capable of the task, but the U3-Axis policy is the most effective, achieving +6.3% improvement in distance and +32% improvement in velocity over the next best policy.

Hammer - Skewed COM and Rectangular Geometry - 15-20 Degree Hand Tilt. The hammer has a skewed COM, located around the intersection of the head and handle. This introduces OOD physics, as torque from gravity applied at the COM (unsupported by the palm) makes the hammer inherently less stable during translation. Also, the handle is rectangular, so there is more contact with the palm, compared to cylinders from training. All policies are capable at 15 degrees, but there is significant performance degradation at 20 degrees. Here, *signed* shear is particularly valuable: the S3-Axis and Signed Shear Only policies achieve the best task metrics. The S3-Axis policy achieves +149% distance and +20% success over the next best policy. Surprisingly, the U3-Axis policy completely failed with this case, and the other policies struggled to manipulate the hammer. The failure modes of the policies are: 1) the policy does not adapt to produce an effective gait within 120 s, or 2) the hammer slips and falls.

Water Bottle - Variable COM and Irregular Geometry - 0-10 Degree Hand Tilt. The water bottle has a variable COM as the water sloshes in the bottle and the bottle geometry is an irregular cylinder. When the hand is tilted and at the beginning of the task, the water is at the bottom of the bottle, which applies a torque on that end. As the water bottle moves across, the COM shifts to the center and eventually to the other end. The most common failure mode is when the policy fails to adapt the finger gait within 120 s. The U3-Axis policy achieves +12.5% distance and +153% velocity over the next best policy.

6.3 Experimental Analysis

Latent Space Analysis. We analyze the extrinsics vector $\hat{z}_t$ from our experiments in Figure 7A with t-SNE to produce 3D plots in Figure 7B. The plots visualize $\hat{z}_t$ from the whole duration of 15 rollouts per policy (5 per object). We find a correlation between high dispersion of $\hat{z}_t$ clusters
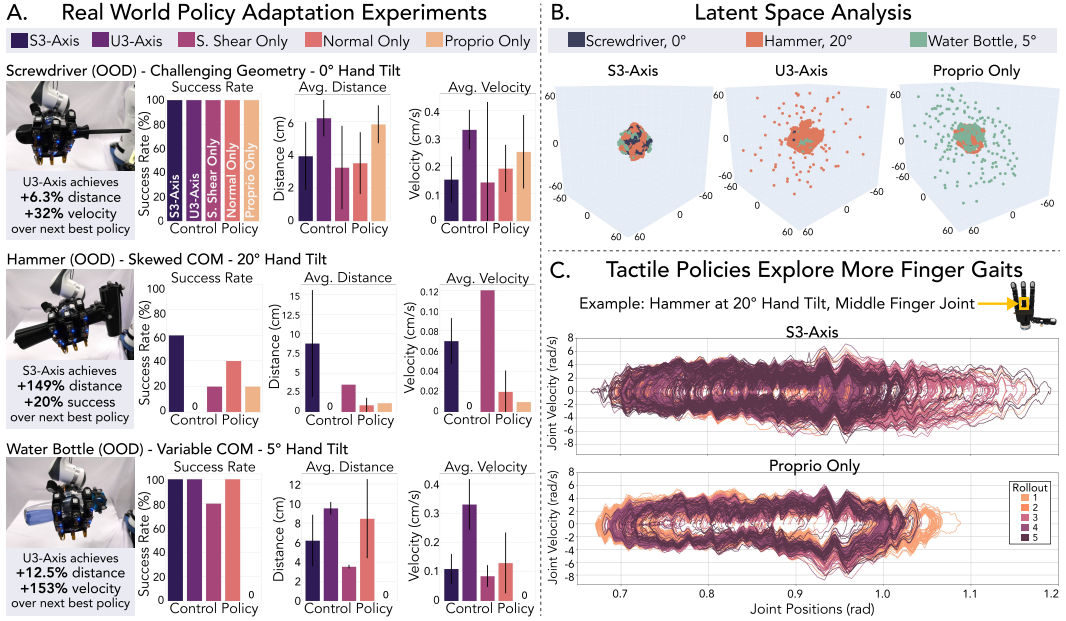
7

Figure 7: **A) Real world policy adaptation experiments.** We highlight experiments near policy adaptation limits, and show that our S3-Axis and U3-Axis policies generally achieve the best task metrics. Water in the bottle is annotated for contrast. **B) Latent space analysis.** We use t-SNE to examine the extrinsics vector $\hat{z}_t$ from our experiments in A. Complete policy failure correlates with high dispersion of $\hat{z}_t$, as shown with U3-Axis and the hammer, and Proprio Only with the water bottle. **C) Tactile policies explore more finger gaits.** These phase portraits show how gaits differ between policies. Intersections through the Poincaré section in the S3-Axis phase portraits have +35% standard deviation compared to Proprio Only.

and complete policy failure. U3-Axis completely failed with the hammer at 20 degrees and Proprio Only completely failed with the water bottle at 5 degrees. The $\hat{z}_t$ clusters for these failed rollouts are more dispersed compared to more successful rollouts. In contrast, the S3-Axis policy was more successful overall and exhibited a dense cluster of $\hat{z}_t$ from all rollouts.

Tactile Policies Explore More Finger Gaits. We analyze the joint states of all policies from our experiments in Figure 7A. We compare the standard deviation of intersections through Poincaré sections of the phase portraits for each finger motor and find that on average, all tactile policies explore more joint states relative to Proprio Only, particularly for the hammer and water bottle experiments. Figure 7C shows the contrast in joint state exploration in phase portraits of S3-Axis and Proprio-Only, where S3-Axis has an increase of 35% standard deviation of intersections through the Poincaré section. Greater joint state exploration is potentially a factor in task success and an indicator of gait adaptation; however, other variables such as gait cycle timing and finger coordination are also important to consider. More analysis is in the Appendix.

Real-World Videos. We show videos of real-world experiments with our methods and ablations on our Project Website. These videos can be used to observe task metrics and policy gait adaptation.

7 Conclusion

In this work, we propose a novel sensor model and show it can be used to train RL policies in simulation for a challenging task. Our dexterous in-hand translation policies with ReSkin can be zero-shot deployed to the real-world. We show that ReSkin shear and normal force sensing consistently enables the best ID performance *and* adaptation to both OOD hand orientations and objects. We see these contributions as a key step towards enabling tactile feedback for general in-hand manipulation.

Limitations and Future Work. We mainly study the new sensor model for touch simulation and learning, and do not consider vision as an input. We will need vision for precise goal-specification. Our control policy is frozen during deployment, but it would be interesting to use real world tactile

feedback to fine tune the policy. We can also investigate domain adaptation methods and sensor simulation improvements for continuous tactile signals, which could enable better performance.

Acknowledgments

References

[1] R. S. Johansson and J. R. Flanagan. Coding and use of tactile signals from the fingertips in object manipulation tasks. *Nature Reviews Neuroscience*, 2009.

[2] M. H. Lee. Tactile sensing: new directions, new challenges. *IJRR*, 2000.

[3] R. D. Howe. Tactile sensing and control of robotic manipulation. *Advanced Robotics*, 1993.

[4] W. Yuan, S. Dong, and E. H. Adelson. Gelsight: High-resolution robot tactile sensors for estimating geometry and force. *Sensors*, 2017.

[5] M. Lambeta, P.-W. Chou, S. Tian, B. Yang, B. Maloon, V. R. Most, D. Stroud, R. Santos, A. Byagowi, G. Kammerer, et al. Digit: A novel design for a low-cost compact high-resolution tactile sensor with application to in-hand manipulation. *RA-L*, 2020.

[6] R. Bhirangi, T. Hellebrekers, C. Majidi, and A. Gupta. Reskin: versatile, replaceable, lasting tactile skins. In *5th Annual Conference on Robot Learning*, 2021.

[7] H. Qi, B. Yi, Y. Ma, S. Suresh, M. Lambeta, R. Calandra, and J. Malik. General in-hand object rotation with vision and touch. In *CoRL*, 2023.

[8] Z.-H. Yin, B. Huang, Y. Qin, Q. Chen, and X. Wang. Rotating without seeing: Towards in-hand dexterity through touch. In *RSS*, 2023.

[9] G. Khandate, S. Shang, E. T. Chang, T. L. Saidi, J. Adams, and M. Ciocarlie. Sampling-based exploration for reinforcement learning of dexterous manipulation. In *RSS*, 2023.

[10] J. Xu, S. Kim, T. Chen, A. R. Garcia, P. Agrawal, W. Matusik, and S. Sueda. Efficient tactile simulation with differentiability for robotic manipulation. In *CoRL*, 2023.

[11] S. Wang, M. Lambeta, P.-W. Chou, and R. Calandra. Tacto: A fast, flexible, and open-source simulator for high-resolution vision-based tactile sensors. *RA-L*, 2022.

[12] Z. Si, G. Zhang, Q. Ben, B. Romero, Z. Xian, C. Liu, and C. Gan. Difftactile: A physics-based differentiable tactile simulator for contact-rich robotic manipulation. *arXiv:2403.08716*, 2024.

[13] D. Ma, E. Donlon, S. Dong, and A. Rodriguez. Dense tactile force estimation using gelslim and inverse fem. In *ICRA*, 2019.

[14] C. Sferrazza, A. Wahlsten, C. Trueeb, and R. D'Andrea. Ground truth force distribution for learning-based tactile sensing: A finite element approach. *IEEE Access*, 2019.

[15] W. Du, W. Xu, J. Ren, Z. Yu, and C. Lu. Tacipc: Intersection-and inversion-free fem-based elastomer simulation for optical tactile sensors. *RA-L*, 2024.

[16] A. A. Cole, P. Hsu, and S. S. Sastry. Dynamic control of sliding by robot hands for regrasping. *IEEE Transactions on robotics and automation*, 1992.

[17] W. Yang and M. Posa. Dynamic on-palm manipulation via controlled sliding. In *RSS*, 2024.

[18] C. Teeple, B. Aktas, M. C.-S. Yuen, G. Kim, R. D. Howe, and R. Wood. Controlling palm-object interactions via friction for enhanced in-hand manipulation. *RA-L*, 2022.

[19] Y. Lin, J. Lloyd, A. Church, and N. F. Lepora. Tactile gym 2.0: Sim-to-real deep reinforcement learning for comparing low-cost high-resolution robot touch. *RA-L*, 2022.

[20] Z. Chen, S. Zhang, S. Luo, F. Sun, and B. Fang. Tacchi: A pluggable and low computational cost elastomer deformation simulator for optical tactile sensors. *RA-L*, 2023.

[21] Z. Si and W. Yuan. Taxim: An example-based simulation model for gelsight tactile sensors. *RA-L*, 2022.

[22] Y. Narang, B. Sundaralingam, M. Macklin, A. Mousavian, and D. Fox. Sim-to-real for robotic tactile sensing via physics-based simulation and learned latent projections. In *ICRA*, 2021.

[23] Q. K. Luu, N. H. Nguyen, et al. Simulation, learning, and application of vision-based tactile sensing at large scale. *T-RO*, 2023.

[24] E. Todorov, T. Erez, and Y. Tassa. Mujoco: A physics engine for model-based control. In *IROS*, 2012.

[25] V. Makoviychuk, L. Wawrzyniak, Y. Guo, M. Lu, K. Storey, M. Macklin, D. Hoeller, N. Rudin, A. Allshire, A. Handa, and G. State. Isaac gym: High performance gpu-based physics simulation for robot learning. In *NeurIPS Datasets and Benchmarks*, 2021.

[26] S. Cremer, M. N. Saadatzi, I. B. Wijayasinghe, S. K. Das, M. H. Saadatzi, and D. O. Popa. Skinsim: A design and simulation tool for robot skin with closed-loop phri controllers. *IEEE Transactions on Automation Science and Engineering*, 2020.

[27] Z. Kappassov, J.-A. Corrales-Ramon, and V. Perdereau. Simulation of tactile sensing arrays for physical interaction tasks. In *IEEE/ASME International Conference on Advanced Intelligent Mechatronics*, 2020.

[28] T. Hellebrekers, O. Kroemer, and C. Majidi. Soft magnetic skin for continuous deformation sensing. *Advanced Intelligent Systems*, 2019.

[29] A. S. Morgan, K. Hang, B. Wen, K. Bekris, and A. M. Dollar. Complex in-hand manipulation via compliance-enabled finger gaiting and multi-modal planning. *RA-L*, 2022.

[30] L. Han and J. C. Trinkle. Dextrous manipulation by rolling and finger gaiting. In *ICRA*, 1998.

[31] J.-P. Saut, A. Sahbani, S. El-Khoury, and V. Perdereau. Dexterous manipulation planning using probabilistic roadmaps in continuous grasp subspaces. In *IROS*, 2007.

[32] D. Rus. In-hand dexterous manipulation of piecewise-smooth 3-d objects. *IJRR*, 1999.

[33] Y. Bai and C. K. Liu. Dexterous manipulation using both palm and fingers. In *ICRA*, 2014.

[34] I. Mordatch, Z. Popović, and E. Todorov. Contact-invariant optimization for hand manipulation. In *Eurographics*, 2012.

[35] R. Fearing. Implementing a force strategy for object re-orientation. In *ICRA*, 1986.

[36] S. P. Arunachalam, I. Güzey, S. Chintala, and L. Pinto. Holo-dex: Teaching dexterity with immersive mixed reality. In *ICRA*, 2023.

[37] S. Haldar, J. Pari, A. Rai, and L. Pinto. Teach a robot to fish: Versatile imitation from one minute of demonstrations. In *RSS*, 2023.

[38] S. P. Arunachalam, S. Silwal, B. Evans, and L. Pinto. Dexterous imitation made easy: A learning-based framework for efficient dexterous manipulation. In *ICRA*, 2023.

[39] Y. Qin, H. Su, and X. Wang. From one hand to multiple hands: Imitation learning for dexterous manipulation from single-camera teleoperation. *RA-L*, 2022.

[40] C. Wang, H. Shi, W. Wang, R. Zhang, L. Fei-Fei, and C. K. Liu. Dexcap: Scalable and portable mocap data collection system for dexterous manipulation. In *RSS*, 2024.

[41] OpenAI, M. Andrychowicz, B. Baker, M. Chociej, R. Józefowicz, B. McGrew, J. Pachocki, A. Petron, M. Plappert, G. Powell, A. Ray, J. Schneider, S. Sidor, J. Tobin, P. Welinder, L. Weng, and W. Zaremba. Learning dexterous in-hand manipulation. *IJRR*, 2019.

[42] OpenAI, I. Akkaya, M. Andrychowicz, M. Chociej, M. Litwin, B. McGrew, A. Petron, A. Paino, M. Plappert, G. Powell, R. Ribas, J. Schneider, N. Tezak, J. Tworek, P. Welinder, L. Weng, Q. Yuan, W. Zaremba, and L. Zhang. Solving rubik's cube with a robot hand. *arXiv:1910.07113*, 2019.

[43] A. Handa, A. Allshire, V. Makoviychuk, A. Petrenko, R. Singh, J. Liu, D. Makoviichuk, K. Van Wyk, A. Zhurkevich, B. Sundaralingam, Y. Narang, J.-F. Lafleche, D. Fox, and G. State. Dextreme: Transfer of agile in-hand manipulation from simulation to reality. In *ICRA*, 2023.

[44] T. Chen, M. Tippur, S. Wu, V. Kumar, E. Adelson, and P. Agrawal. Visual dexterity: In-hand dexterous manipulation from depth. *Science Robotics*, 2023.

[45] T. Lin, Z.-H. Yin, H. Qi, P. Abbeel, and J. Malik. Twisting lids off with two hands. *arXiv:2403.02338*, 2024.

[46] H. Qi, A. Kumar, R. Calandra, Y. Ma, and J. Malik. In-hand object rotation via rapid motor adaptation. In *CoRL*, 2022.

[47] M. Yang, C. Lu, A. Church, Y. Lin, C. Ford, H. Li, E. Psomopoulou, D. A. Barton, and N. F. Lepora. Anyrotate: Gravity-invariant in-hand object rotation with sim-to-real touch. *arXiv preprint arXiv:2405.07391*, 2024.

[48] K. M. Lynch and F. C. Park. *Modern robotics*. Cambridge University Press, 2017.

[49] J. Schulman, F. Wolski, P. Dhariwal, A. Radford, and O. Klimov. Proximal policy optimization algorithms. *arXiv:1707.06347*, 2017.

[50] WonikRobotics. Allegrohand. https://www.wonikrobotics.com/, 2013.

A Demonstrations

A.1 Generalization to Diverse Objects

We demonstrate the generalization of our 3-axis tactile policies to diverse objects, outside of the 4 real world objects in our test set. Please see the supplemental video for footage.

Figure 8: Demonstrations with diverse objects outside of our main test set. All items are being manipulated by either the U3-Axis policy or the S3-Axis policy. The weights of the objects range from 57 g (paper towel roll) to 524 g (rolling pin).

A.2 Real ReSkin and U3-Axis Model Comparison

Here, we compare our U3-Axis tactile skin model to a representative example of real ReSkin. This is the same taxel and same rollout as the examples shown in Figure 3.

Figure 9: Tactile signal comparisons for one taxel during an entire episode of in-hand translation for U3-Axis and real ReSkin.

B Experiments

B.1 Object Dataset

1. *Cylinder (ID).* This 3D printed uniform cylinder evaluates the policy on an ID object. It has a 6.5 cm diameter and 22.2 cm length, weighing 108 g.
2. *Hammer (OOD).* The hammer tests adaptation to a skewed COM and rectangular handle geometry. It is 3D printed and inspired by a real hammer from McMaster-Carr[1]. All dimensions are scaled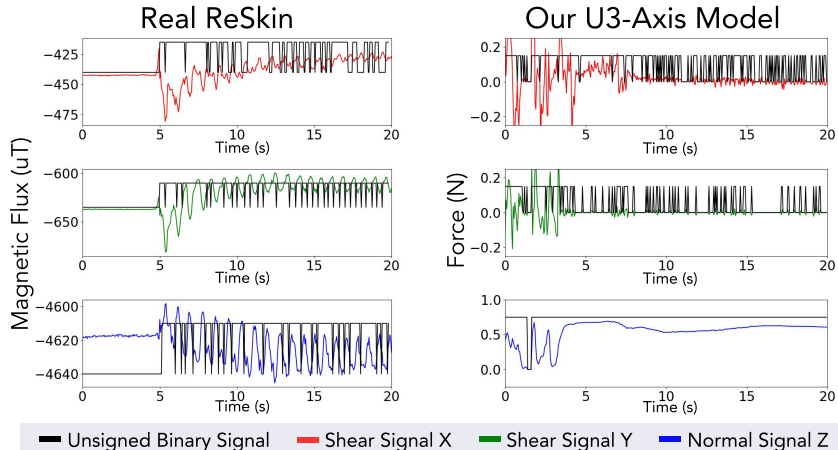 by 200% to match the scale of an Allegro Hand compared to a human hand. It has a total length of 37 cm, and the handle is 6.1 cm by 4.3 cm. The hammer head is 20 cm by 4.8 cm by 6.4 cm. The total weight is 284 g.
3. *Screwdriver (OOD).* The screwdriver evaluates adaptation to complex geometry and multiple contacts. It is 3D printed and inspired by a real screwdriver from McMaster-Carr[2], also scaled by 200%. The handle diameters range from 3.8 cm to 5.4 cm, and the handle is 23.4 cm. The total length is 39.4 cm, and it weighs 180 g.
4. *Water Bottle (OOD).* The water bottle tests adaptation to a variable COM and non-uniform cylindrical geometry. The water bottle diameter ranges from 6 to 7 cm, and the total weight is 252 g. It contains 191 g of water.

B.2 Real World Evaluation Results

Summary tables for all real world experiments are reported below.

Water Bottle - Variable COM				
Hand Tilt	Policy	Success (of 5) ↑	Avg. Dist. (cm) ↑	Avg. Vel. (cm/s) ↑
0 deg.	**Signed 3-Axis**	100	9.38 ± 1.61	0.08 ± 0.07
	Unsigned 3-Axis	100	8.13 ± 0.83	0.27 ± 0.02
	Signed Shear Only	100	5.57 ± 4.70	0.08 ± 0.11
	Normal Only	100	8.17 ± 0.33	0.1 ± 0.02
	Proprioception Only	100	10.76 ± 0.64	0.13 ± 0.08
5 deg.	**Signed 3-Axis**	100	6.20 ± 2.63	0.11 ± 0.051
	Unsigned 3-Axis	100	9.50 ± 0.64	0.33 ± 0.09
	Signed Shear Only	80	4.71 ± 0.19	0.08 ± 0.04
	Normal Only	100	8.44 ± 4.05	0.13 ± 0.10
	Proprioception Only	0	0	0
10 deg.	**Signed 3-Axis**	100	1.36 ± 1.63	0.03 ± 0.03
	Unsigned 3-Axis	0	0	0
	Signed Shear Only	0	0	0
	Normal Only	0	0	0
	Proprioception Only	0	0	0

Table 1: Results for policy adaptation with the water bottle. Success out of 5 trials, translation distance averaged over successful trials, object velocity averaged over successful trials.

---

[1]https://www.mcmaster.com/5914A15/
[2]https://www.mcmaster.com/7127A34/

		Cylinder - ID Object		
Hand Tilt	Policy	Success (of 5) ↑	Avg. Dist. (cm) ↑	Avg. Vel. (cm/s) ↑
0 deg.	**Signed 3-Axis**	100	$7.43_{\pm0.19}$	$0.33_{\pm0.01}$
	Proprioception Only	100	$5.39_{\pm1.61}$	$0.17_{\pm0.07}$
5 deg.	**Signed 3-Axis**	100	$7.1_{\pm0.47}$	$0.34_{\pm0.02}$
	Proprioception Only	100	$4.25_{\pm0.95}$	$0.05_{\pm0.05}$
10 deg.	**Signed 3-Axis**	100	$7.62_{\pm0.32}$	$0.22_{\pm0.02}$
	Proprioception Only	100	$3.72_{\pm0.71}$	$0.06_{\pm0.02}$
15 deg.	**Signed 3-Axis**	100	$2.66_{\pm0.96}$	$0.042_{\pm0.01}$
	Proprioception Only	40	$0.16_{\pm0.15}$	$0.001_{\pm0.003}$

Table 2: Results for policy adaptation with the cylinder. Success out of 5 trials, translation distance averaged over successful trials, object velocity averaged over successful trials.

		Hammer - Skewed COM		
Hand Tilt	Policy	Success (of 5) ↑	Avg. Dist. (cm) ↑	Avg. Vel. (cm/s) ↑
15 deg.	**Signed 3-Axis**	100	$12.53_{\pm1.08}$	$0.23_{\pm0.21}$
	Unsigned 3-Axis	100	$5.30_{\pm4.40}$	$0.05_{\pm0.11}$
	Signed Shear Only	100	$6.55_{\pm1.35}$	$0.25_{\pm0.05}$
	Normal Only	100	$7.36_{\pm5.93}$	$0.14_{\pm0.16}$
	Proprioception Only	100	$11.33_{\pm1.02}$	$0.23_{\pm0.02}$
20 deg.	**Signed 3-Axis**	100	$6.20_{\pm2.63}$	$0.11_{\pm0.051}$
	Unsigned 3-Axis	100	$9.50_{\pm0.64}$	$0.33_{\pm0.09}$
	Signed Shear Only	80	$4.71_{\pm0.19}$	$0.08_{\pm0.04}$
	Normal Only	100	$8.44_{\pm4.05}$	$0.13_{\pm0.10}$
	Proprioception	0	0	0

Table 3: Results for policy adaptation with the hammer. Success out of 5 trials, translation distance averaged over successful trials, object velocity averaged over successful trials.

		Screwdriver - Challenging Geometry		
Hand Tilt	Policy	Success (of 5) ↑	Avg. Dist. (cm) ↑	Avg. Vel. (cm/s) ↑
0 deg.	**Signed 3-Axis**	100	$3.91_{\pm0.08}$	$0.23_{\pm0.08}$
	Unsigned 3-Axis	100	$6.19_{\pm1.09}$	$0.33_{\pm0.07}$
	Signed Shear Only	100	$3.22_{\pm2.5}$	$0.14_{\pm0.29}$
	Normal Only	100	$3.49_{\pm1.86}$	$0.19_{\pm0.09}$
	Proprioception Only	100	$5.82_{\pm1.14}$	$0.25_{\pm0.13}$

Table 4: Results for policy adaptation with the screwdriver. Success out of 5 trials, translation distance averaged over successful trials, object velocity averaged over successful trials.

B.3 Gait Analysis

We show the phase portraits of the middle finger motor for all policies evaluated in the Hammer, 20 degree hand tilt experiment. For this specific example, we analyze joint state exploration by measuring the standard deviation of intersections through the Poincarè section, which is a plane through joint velocity = 0 and joint angle < 0.9. Here, S3-Axis has +35% greater deviation, U3-Axis has +18% deviation, Signed Shear Only has +26% deviation, and Normal Only has -40% deviation, relative to Proprio Only. Although Normal Only is the exception here, we find that on

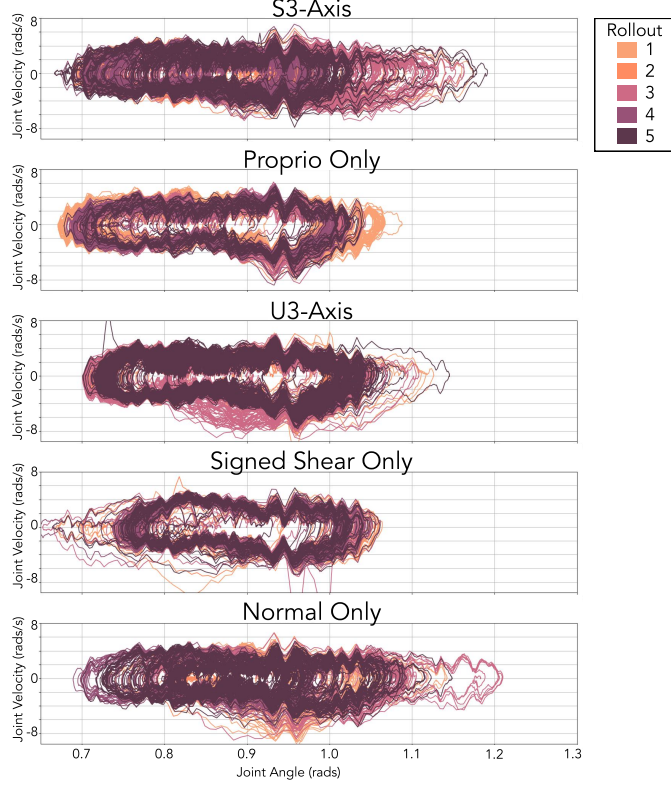average with the highlighted experiments in Figure 7, tactile policies generally explore more joint states.

Figure 10: Phase portraits of the middle finger motor, for all policies evaluated for the hammer at 20 degrees.

C   Implementation Details

C.1   Reward Function

This is the reward function we use to train the oracle policy:

$$r \doteq r_{\text{iht}} + \lambda_{\text{rotp}} r_{\text{rotp}} + \lambda_{\text{goal}} r_{\text{goal}} + \lambda_{\text{drop}} r_{\text{drop}} + \lambda_{\text{pose}} r_{\text{pose}} + \lambda_{\text{work}} r_{\text{work}} + \lambda_{\text{torque}} r_{\text{torque}} + \lambda_{\text{force}} r_{\text{force}} \quad (1)$$

The in-hand translation task is defined as $r_{\text{iht}} \doteq -(x_{\text{obj\_pos}} - x_{\text{obj\_goal\_pos}})^2$, where $x_{\text{obj\_pos}}$ is the object's current position and $x_{\text{obj\_goal\_pos}}$ is the object's goal position. In this work, randomized goal positions are a curriculum to produce a versatile, robust finger gait. However, using only this reward term results in policies that exploit inaccurate sliding contact simulation that do not transfer from sim-to-real. Thus, we add additional penalties on object state. $r_{\text{rotp}} \doteq -(x_{\text{obj\_left\_end}} - x_{\text{obj\_right\_end}})^2$ penalizes object rotation, $r_{\text{goal}} \doteq (1 \text{ if } \sqrt{(x_{i,\text{obj\_pos}} - x_{i,\text{obj\_goal\_pos}})^2} < \epsilon \text{ else } 0)$ as another reward when the object reaches the goal position, and $r_{\text{drop}} \doteq \min(\max((x_{\text{obj\_pos}} - x_{\text{threshold}}), -1), 0)$ to penalize dropping the object.

For the emergence of the finger gait, we use the following penalty terms on the robot hand, similar to [46, 7]: $r_{\text{pose}} \doteq -||q - q_{\text{init}}||_2^2$ to penalize finger pose deviation, $r_{\text{work}} \doteq -\tau^T \dot{q}$ to penalize energy consumption, $r_{\text{torque}} \doteq -||\tau||_2^2$ to penalize applied finger torque, where. Furthermore, we add $r_{\text{force}} \doteq -\frac{1}{4} \sum_{i=1}^4 (F_i - \mu)^2$ to penalize the variance of forces applied by all fingers, where F_i is the total force applied by all rigid bodies in one finger, i corresponds to each finger, and μ is the mean force of all fingers. We empirically found this term to encourage policy behaviors that transfer well to the real world.

C.2 Hyperparameters

Reward Function

Reward Term	Scale, λ
r_{iht}	700
r_{rotp}	500
r_{goal}	10
r_{drop}	1000
r_{pose}	-0.3
r_{work}	-2.0
r_{torque}	-0.1
r_{force}	500

Table 5: Reward scales for the oracle policy.

Simulation Physics

Parameter	Randomization Range or Value
Object Scales	$[0.7, 1.2]$
Object Mass	$[0.1, 0.35]$ kg
Object Center of Mass (COM)	$[-0.01, 0.01]$ m
Coefficient of Friction	$[0.3, 3.0]$
PD Controller Stiffness	$[2.9, 3.1]$
PD Controller Damping	$[0.09, 0.11]$
Contact Offset	0.002
Bounce Threshold Velocity	0.2 m/s
Max Depenetration Velocity	1.0 m/s

Table 6: Physics parameters for policy training in simulation. For the object scales, the range is discretized by 0.02 and the scales are applied to one canonical cylinder.

Tactile Skin Simulation

Term	Value
Sensing Range Threshold (Beyond Taxel)	1 cm
Sensing Range Randomization	15%
Sensor Noise	3%
Threshold for Binary Values	0.0005 N

Table 7: Parameters for our tactile skin model implemented in IsaacGym.

Binary Filter for Real ReSkin

Axis	Threshold	Current Buffer Size	History Buffer Size	Filter Window	Filter α
X (Shear)	0.75	10	50	10	0.4
Y (Shear)	0.7	10	50	10	0.4
Z (Normal)	0.67	10	50	10	0.4

Table 8: Binarization filter parameters for real ReSkin, which uses two buffers to calculate the time derivative of the signals. We smooth all raw ReSkin inputs with an exponential moving average filter prior to input to the buffers, and the window size and α smoothing parameter is reported above.

C.3 Training Settings

Simulation Settings. When training the oracle policy, we use 32768 parallel environments, distributed on 4 GPUs, to train the agent. Each environment contains a simulated Allegro Hand, simulated ReSkin palm collision geometries, a cylinder with randomized parameters (Table 6), as well as random initial and goal positions. The ReSkin palm tactile outputs are not simulated for the oracle policy, but we include the collision geometries for the oracle policy, to have consistent dynamics when training the student policy. The simulation frequency is 200 Hz, the control frequency is 20 Hz, each episode lasts for 400 control steps (20 s). The wall clock time for oracle policy training is 1.68 days.

When training the tactile and proprioceptive policies, we simulate the ReSkin palm outputs (Table 7), and instead we use 1000 parallel environments distributed across 2 GPUs. Unless mentioned otherwise, the simulation settings are the same as the oracle policy. The wall clock time for training the student policy with tactile skin simulation is 6.27 hours.

Stable Grasp Generation. Both the oracle and tactile policies assume that the object is initialized in a stable grasp, similar to [46, 7]. We pre-generate caches of stable grasp poses for training.

First, we define canonical poses for the fingers, which varies for each scale of the object. Because we train for a large range of scales, the same canonical pose will not work for the entire range. Then, we define a range of relative offsets within $[-0.25, 0.25]$ rad to randomly sample from. Additionally, we define a canonical position for the object and sample from a relative offset of $[-10, 10]$ cm along the x-axis for the object. The canonical object pose is the same for all scales: $[x, y, z, w_{\text{quat}}, x_{\text{quat}}, y_{\text{quat}}, z_{\text{quat}}] = [0, 0, 0.52, 0, -0.5, 0, 0.5]$.

We let the simulation run for 0.5 s. The finger and object positions are saved (i.e., deemed a stable grasp) if the following conditions are satisfied:

1. All fingertips are within 10 cm of the object.
2. At least 2 fingers are in contact with the object.
3. The object did not fall below the hand.
4. The object is in contact with the palm.

We sampled 50,000 grasps and object poses for each object scale.

Goal Generation. The goal position for the object is sampled from a range of relative offsets $[3, 10]$ cm along the x-axis from the object's canonical pose. The minimum offset is 3 cm to encourage meaningful object translation, and the maximum is 10 cm which is at the end of the canonical cylinder length.

C.4 Hardware Setup

We place a 0.25mm sheet of PET-like plastic on top of the ReSkin palm to reduce friction between the sensing skin and the object. Reducing the friction will reduce the required torque from the fingers to move the object; this avoids overheating the motors. The plastic sheet is not adhered to the sensing skin.

We also place high-friction 3M tape (3M 300LSE) at the base of thumb and index finger motors. This reduces object slip and somewhat helps with object translation, since the policy sometimes pinches the object between these fingers during part of the finger gait. We also cover the outside casing of the fingertips with the same 3M tape, although they typically do not contact the object.
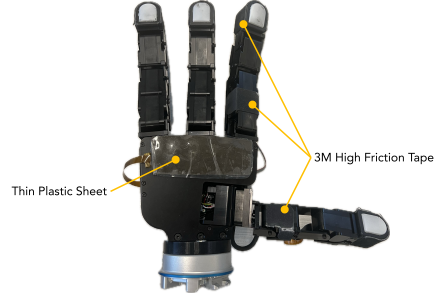

Figure 11: Friction modifications for Allegro Hand and ReSkin.